The Planetary Science Journal, 3:75 (13pp), 2022 April https://doi.org/10.3847/PSJ/ac5597
© 2022. The Author(s). Published by the American Astronomical Society.
OPEN ACCESS

Geologic Context of the OSIRIS-REx Sample Site from High-resolution Topography and Imaging

O. S. Barnouin[1], E. R. Jawin[2], R. T. Daly[1], R.-L. Ballouz[1], M. G. Daly[3], J. A. Seabrook[3], P. Michel[4], Y. Zhang[4], C. L. Johnson[5,6], K. J. Walsh[7], M. M. Al Asad[5], R. Gaskell[6], J. Weirich[6], E. Palmer[6], E. B. Bierhaus[8], M. C. Nolan[9], C. W. V. Wolner[9], and D. S. Lauretta[9]

[1] The Johns Hopkins University Applied Physics Laboratory, Laurel, MD 20723-6099, USA; olivier.barnouin@jhuapl.edu
[2] Smithsonian National Air and Space Museum, Washington, DC 20560, USA
[3] The Centre for Research in Earth and Space Science, York University, Toronto, ON, Canada
[4] Université Côte d'Azur, Observatoire de la Côte d'Azur, CNRS, Laboratoire Lagrange, CS 34229, F-06304 Nice Cedex 4, France
[5] Univ. of British Columbia, Vancouver, BC, Canada
[6] Planetary Science Institute, Tucson, AZ 85719, USA
[7] Southwestern Research Institute, Boulder, CO 80302, USA
[8] Lockheed Martin Space, Littleton, CO 80125, USA
[9] Lunar and Planetary Laboratory, University of Arizona, Tucson, AZ 85721, USA
Received 2021 October 7; revised 2022 February 7; accepted 2022 February 14; published 2022 April 5

Abstract

The OSIRIS-REx spacecraft collected a surface sample from Hokioi crater (55.8° N, 42.3° E; diameter ∼20 m) on the asteroid Bennu in 2020 October. We explore the geology of the sample collection site, known as Nightingale, by using digital terrain models, relative albedo maps, and images collected by the OSIRIS-REx spacecraft. Hokioi crater sits at the northwest edge of an older, larger (120 m diameter) crater between two north–south ridges respectively located at roughly 0° and 90° longitude, between which unconsolidated material generally migrates from the geopotential high at the north (+*Z*) pole to the geopotential low at the equator. The impact that formed Hokioi crater exposed relatively unweathered, fine-grained dark material that we observe within and ejected beyond the crater. The regional slope and steep crater walls to the north of the Nightingale site have enabled a mix of the dark debris and brighter material (which may include carbonates and/or exogenic basalts) surrounding Hokioi crater to migrate onto the crater floor, where the sample was collected; some of this material may be old ejecta excavated from up to 10 m depth when the 120 m diameter crater formed. We therefore expect the OSIRIS-REx sample to include materials of varying brightnesses, compositions, and exposure ages, derived primarily from the 0°–90° longitude quadrant and from as deep as 10 m. The sample may also include material derived from the impactor that formed Hokioi crater. We expect it to have low cohesion (≪0.6 Pa) and a friction angle between 32° and 39°.

Unified Astronomy Thesaurus concepts: Asteroids (72); Asteroid surfaces (2209)

1. Introduction

Following a survey of asteroid (101955) Bennu that included several flybys and orbital phases, the Origins, Spectral Interpretation, Resource Identification, and Security–Regolith Explorer (OSIRIS-REx) spacecraft collected a surface sample from the asteroid on 2020 October 20, which it will return to Earth in 2023 (Lauretta et al. 2021).

The OSIRIS-REX instruments include a camera suite (OCAMS; Rizk et al. 2018; Golish et al. 2020), a laser altimeter (OLA; Daly et al. 2017), visible and infrared spectrometers (OVIRS and OTES; Reuter et al. 2018; Christensen et al. 2018), and an X-ray spectrometer (REXIS; Masterson et al. 2018). The data collected during the survey and orbital phases revealed a rugged, boulder-rich surface (Lauretta et al. 2019; Burke et al. 2021). Variations in surface color and albedo indicate different exposure ages (where darker, spectrally redder material is fresher), primordial heterogeneity in the form of two primary boulder populations (dark and rough versus brighter and smooth), and a minor population of exogenic basaltic materials (DellaGiustina et al. 2020, 2021). Bennu's composition is consistent with that of the aqueously altered CM and CI meteorites and includes hydrated Mg-rich phyllosilicates, magnetite, carbonates, organic compounds, and a minor component of anhydrous silicates (Hamilton et al. 2019; Lauretta et al. 2019; Kaplan et al. 2020; Simon et al. 2020; Hamilton et al. 2021). Observations by OCAMS and OLA have enabled the construction of high-resolution global digital terrain models (GDTMs; Barnouin et al. 2020) of the asteroid with ground sample distances (GSDs) of 0.2 m. These GDTMs reveal that Bennu is a top-shaped, rubble-pile asteroid (Barnouin et al. 2019; Daly et al. 2020a), made from reaccumulated fragments of a larger parent body that was catastrophically disrupted (Michel et al. 2020). Bennu possesses broad north–south longitudinal ridges that extend in some instances across nearly all latitudes of the asteroid; although these ridges are muted and can be difficult to discern, they are evident in spherical harmonic analyses, both global and hemispherical, of the shape of Bennu (Barnouin et al. 2019; Daly et al. 2020a; Roberts et al. 2021). These ridges explain the diamond shape of Bennu that becomes apparent when the asteroid is viewed from the poles (Barnouin et al. 2019).

Bennu shows evidence for internal stiffness (Barnouin et al. 2019). Its shape can be sustained by friction angles of <18°

Original content from this work may be used under the terms of the Creative Commons Attribution 4.0 licence. Any further distribution of this work must maintain attribution to the author(s) and the title of the work, journal citation and DOI.

(Barnouin et al. 2019; Roberts et al. 2021), or bulk cohesion of ~1 Pa (Scheeres et al. 2019; Roberts et al. 2021). The density of Bennu is heterogeneous, with lower densities at its center and along its equatorial bulge (Scheeres et al. 2019). The OCAMS and OLA data, combined with surface slope estimates (Scheeres et al. 2019, 2020), indicate that Bennu has an active, dynamic surface on which material migrates from the areas of high elevation near the poles to areas of low elevation at the equator (Daly et al. 2020a; Jawin et al. 2020; Barnouin et al. 2022). In the southern hemisphere, an abundance of large boulders has impeded this migration, thereby creating a north–south asymmetry in the asteroid shape, with the southern ($-Z$) hemisphere having a more rounded appearance than the northern ($+Z$) hemisphere (Daly et al. 2020a). Observations of the migrations of surface material constrain cohesion in the upper 3–10 m beneath Bennu's surface to a very small value of <0.2 Pa (Barnouin et al. 2022).

The sample collection site, named Nightingale, is positioned inside the 20 m diameter Hokioi crater located at 42.3° E, 55.8° N. Here, we constrain the geological evolution and characterize the local physical nature of the Nightingale sample site in Hokioi crater. Important clues to the area's evolution come from high-resolution GDTMs and local DTMs (LDTMs) (GSD $\leqslant$ 0.05 m), a global image mosaic (Bennett et al. 2021), and the relative albedo at 1064 nm measured by OLA. We also discuss the setting of the Nightingale site with respect to Bennu's global geology (Jawin et al. 2022). All these data provide insight into the origins of the material collected by the OSIRIS-REx spacecraft.

2. Data Sets Analyzed

2.1. Digital Terrain Models

We used DTMs constructed in two different ways for our analysis. First, we used DTMs generated from OLA range measurements collected during one of the orbital phases of the OSIRIS-REx mission (Daly et al. 2020a). These included GDTMs that sample the asteroid from 12 to 0.8 m GSD and a global set of LDTMs that sample the asteroid down to 0.2 m GSD. The individual vertices that compose these DTMs represent the asteroid size with a radial uncertainty $\leqslant$0.15 m (Daly et al. 2020a). These models provide information on the global and regional geological context of the sample site. We also analyzed a high-resolution OLA LDTM of the Nightingale site with a GSD of 0.05 m and a point-to-point uncertainty (precision) of <0.0175 m. This LDTM's GSD of 0.05 m is just less than the size of the OLA laser spot size (~0.07 m) collected in the region of the LDTM, but it is a useful estimate of the resolution given that each 0.05×0.05 m bin had a median of 10 OLA returns.

Second, to assess attributes of the sample site at even finer scales, we combined stereophotoclinometry (SPC; Gaskell et al. 2008) of image data with ranging measurements from OLA to generate an "SPO" LDTM (Barnouin et al. 2020), which sampled the surface of the Nightingale site at 0.01 m GSD. The data that went into making this LDTM include high-resolution images from OCAMS (near 0.003 m pixel^{-1}) and much lower resolution data (~0.5 m pixel^{-1}) from TAGCAMS (the spacecraft's Touch And Go Camera System; Bos et al. 2018, 2020). The OLA measurements provided weighted constraints to the broader shape of this SPO product, including better measurements of rock heights than from SPC alone. The precision of the 0.01 m LDTM is $\leqslant$0.0176 m, or about the same uncertainty as the OLA 0.05 m LDTM. Our experience with such SPO products has shown that uncertainties are highest at large rocks, where surface slope changes rapidly.

We also used maps of elevation and slopes. Elevation, also known as geopotential altitude (Scheeres et al. 2016), is computed as the difference between the gravitational surface potential and a reference potential divided by the magnitude of the local gravitational acceleration g, considering the asteroid mass and spin rate (Cheng et al. 2002; Barnouin-Jha et al. 2008). It is essentially equivalent to a measure of topography on Earth. Slope is the angle between the surface normal vector and the gravity vector (Barnouin et al. 2020). For the sake of numerical expedience, these values are computed solely from the shape using a uniform bulk density of 1194 ± 3 kg m^{-3} (Daly et al. 2020a) for Bennu. Use of the measured variable gravity or density estimates from Scheeres et al. (2020) would result in modest differences in slope ($\leqslant 1\overset{\circ}{.}0$) and elevation ($\leqslant$1.2% across the entire asteroid; Barnouin et al. 2020) relative to the slopes and elevations estimated using the uniform density model.

2.2. OLA Albedo

In addition to measuring the range to the surface, OLA produces a peak-amplitude measurement of the returned pulse that can be mapped over the surface of Bennu (Daly et al. 2017; Neumann et al. 2020). Because OLA only measures peak pulse amplitude and not the integrated energy received from the surface (a choice made in instrument design to prioritize ranging precision), the map is not strictly a measurement of albedo. Surface roughness over the size of a ~0.07 m laser spot can stretch the pulse and lower the peak amplitude for the same energy. A similar effect can occur for large incident or emission angles. For our purposes here, we refer to this data set as "OLA albedo," recognizing that it can also be indicative of other effects.

Owing to detector limitations, individual OLA peak-amplitude measurements have a low signal-to-noise ratio. An OLA albedo map was nevertheless obtained by using OLA peak-amplitude measurements for ranges to the surface $\leqslant$750 m and emission angles below 45°. The shorter ranges increase the strength of the signal received, while low emission angles minimize the spread of the OLA footprint and, therefore, surface scattering losses. The OLA peak-amplitude measurements used to assess the Nightingale site context thus were limited to data collected in the orbital phases by OLA's low-energy laser transmitter. To reduce noise in the OLA peak-height measurements further, data were averaged over a radius of $\geqslant$0.6 m using a median filter to minimize outliers. This limited the spatial resolution of OLA albedo maps to GSDs of $\geqslant$0.8 m. The emission angle constraint did not allow OLA peak-amplitude measurements to be made from highly tilted surfaces such as the sides of boulders.

The global distribution of peak-amplitude measurements from OLA was scaled to be consistent with the albedo measured by OCAMS (DellaGiustina et al. 2020). This was achieved by normalizing the OLA albedo product such that its distribution peak and limits matched those measured by OCAMS (Daly et al. 2020a).

2.3. Image Mosaic

A global high-resolution mosaic (Bennett et al. 2021), comprising images collected by the PolyCam telescopic imager of OCAMS, facilitated the geologic analysis of the Nightingale sample site by providing regional context that complemented the data provided by the DTMs and OLA albedo. This mosaic has a pixel scale of ∼0.05 m and a mean horizontal position accuracy of ∼0.30 m and was photometrically normalized to 30° phase angle using a Minnaert phase angle correction.

2.4. Global Geologic Map

Lastly, we used a global geologic map of Bennu that was created using the global high-resolution image mosaic, a supplementary lower-resolution basemap (DellaGiustina et al. 2019), and the global set of 0.2 m scale OLA LDTMs (Jawin et al. 2022). Two geologic units are identified in this map, the "Smooth" and "Rugged" Units, which differ in surface texture, concentrations of boulders, and distributions of lineaments, mass movement features, and craters. The units are bounded by several scarps.

The Rugged Unit contains abundant boulders and signs of recent mass movement (Jawin et al. 2022). It also contains fewer small (⩽20 m), putatively fresh craters than the Smooth Unit. The crater retention age of the global surface of Bennu is estimated to be ∼10–65 million years (Bierhaus et al. 2022); on the basis of the distribution of mass movement features and the freshest craters, Jawin et al. (2022) argue that the Smooth Unit has not been significantly resurfaced in the past 2 million years, whereas the Rugged Unit has experienced resurfacing within the past ∼500,000 yr during Bennu's lifetime as a near-Earth asteroid. Thus, the Rugged Unit comprises younger surfaces than the Smooth Unit.

3. Global Context of the Nightingale Site

The 20 m diameter Hokioi crater that contains the Nightingale site is located in the northern hemisphere of Bennu (∼55° N), where longitudinally averaged slopes are the steepest, exceeding 23° (Daly et al. 2020a). The GDTM shows that elevation decreases with latitude, despite an increase in radius due to the equatorial bulge: any mobilized unconsolidated material likely moves across the latitude of Nightingale from the north (+Z) pole toward the equator.

Hokioi crater is located between two broad longitudinal ridges that span most of the asteroid's length from the north to the south pole (Barnouin et al. 2019; Daly et al. 2020a; Roberts et al. 2021). These ridges are located near 0° and 90° E longitude (Figure 1(a)) and stand slightly above the rest of the asteroid (Barnouin et al. 2019; Daly et al. 2020a). They are probably slightly stiffer (Barnouin et al. 2019) and more difficult to degrade than the comparatively low-lying terrain where Hokioi crater is located. The ridges ensure that loose, unconsolidated material at Nightingale comes from within the 0° to 90° E longitudinal quadrant.

Hokioi crater lies within a larger, unnamed impact crater ∼120 m in diameter, confirmed in topography assessments by Daly et al. (2020b). Centered at approximately 60° E, 60° N, this larger crater impinges on the broad-scale, north–south-oriented trough located between the longitudinal ridges, as mapped by Jawin et al. (2022). This crater likely acts as a regional sedimentary basin, trapping and retaining material within its interior. The retention of material is apparent visually toward the southern rim of this large crater, where the number density of boulders is greater than the surroundings (Figure 1(a)). These boulders, along with other sediments, likely have been mobilized into the crater interior by the regional slopes oriented toward the equator. The accumulated sediments seem to have been slowed or prevented from leaving the 120 m crater because the southern crater rim acts as a barrier against further equatorial migration. The southern crater rim has near-zero slopes, rather than a slope reversal (Figure 1(g)). Nevertheless, this flattening is sufficient to slow material that has been mobilized at higher latitudes.

Trapped in the low-lying area between the 120 m crater's western rim and the western longitudinal ridge near 0° E longitude is an elongate concentration of boulders (indicated by a white arrow in Figure 1) that is part of the Rugged Unit (Jawin et al. 2022). Although this accumulation of boulders does not appear to be contributing material to either the 120 m crater or Hokioi crater, it demonstrates that downslope surface motion takes place in this region.

4. Regional Context of the Nightingale Site

The regional geologic setting of the Nightingale site (Figure 2) includes the northern portion of the 120 m crater, Hokioi crater and two similarly sized (∼20 m diameter) craters to its east, and a long latitudinal terrace (Barnouin et al. 2022) just north of Hokioi crater that spans from the rugged terrain in the west to the smooth terrain in the east. The slope immediately north of this terrace generally exceeds 23° over 60° E of longitude (Figure 2). Higher-resolution DTMs show that localized slopes often exceed the angle of repose of granular materials such as sand (∼34°) and gravel (∼45°; Al-Hashemi & Al-Amoudi 2018), which in the absence of cohesion could lead to the surface failing. The OLA albedo data (Figure 2(d)) indicate that Hokioi crater lies in a dark region, probably of its own making, surrounded by brighter terrain to the east and north, as well as in a north–south-elongated bright deposit to the west that appears fan-like in shape. A bright boulder is located at the north end of the bright deposit.

The steep slope, terrace, and bright fan-like deposit indicate that this region of Bennu has likely experienced recent surface creep. Terraces on Bennu result from either surface failure or compression that causes a break in surface slopes (Figures 2(a)–(b)), generating a step-like structure (Barnouin et al. 2022). This process occurs because of ongoing steepening of the surface slopes caused by Bennu's gradually accelerating rotation (Hergenrother et al. 2019; Nolan et al. 2019), which is driven by thermally driven torques known as the Yarkovsky−O'Keefe−Radzievskii−Paddack (YORP; Rubincam 2000) effect. The increase in slope may also explain the formation of the bright deposit in Figure 2(d): the bright deposit seems to originate from the very bright boulder, which we infer may be fragmented in situ, with its fragments tumbling downslope and spreading longitudinally with increasing distance from their source.

Although relatively bright material also exists to the north and east of Hokioi crater, several observations support our inference that the bright boulder has been disrupted and thus is a plausible source of the fan-shaped OLA albedo feature. In Figure 3, we show a PolyCam image of the bright boulder and a high-resolution LDTM colored by height relative to the best-fit plane. We measured two topographic profiles of the boulder

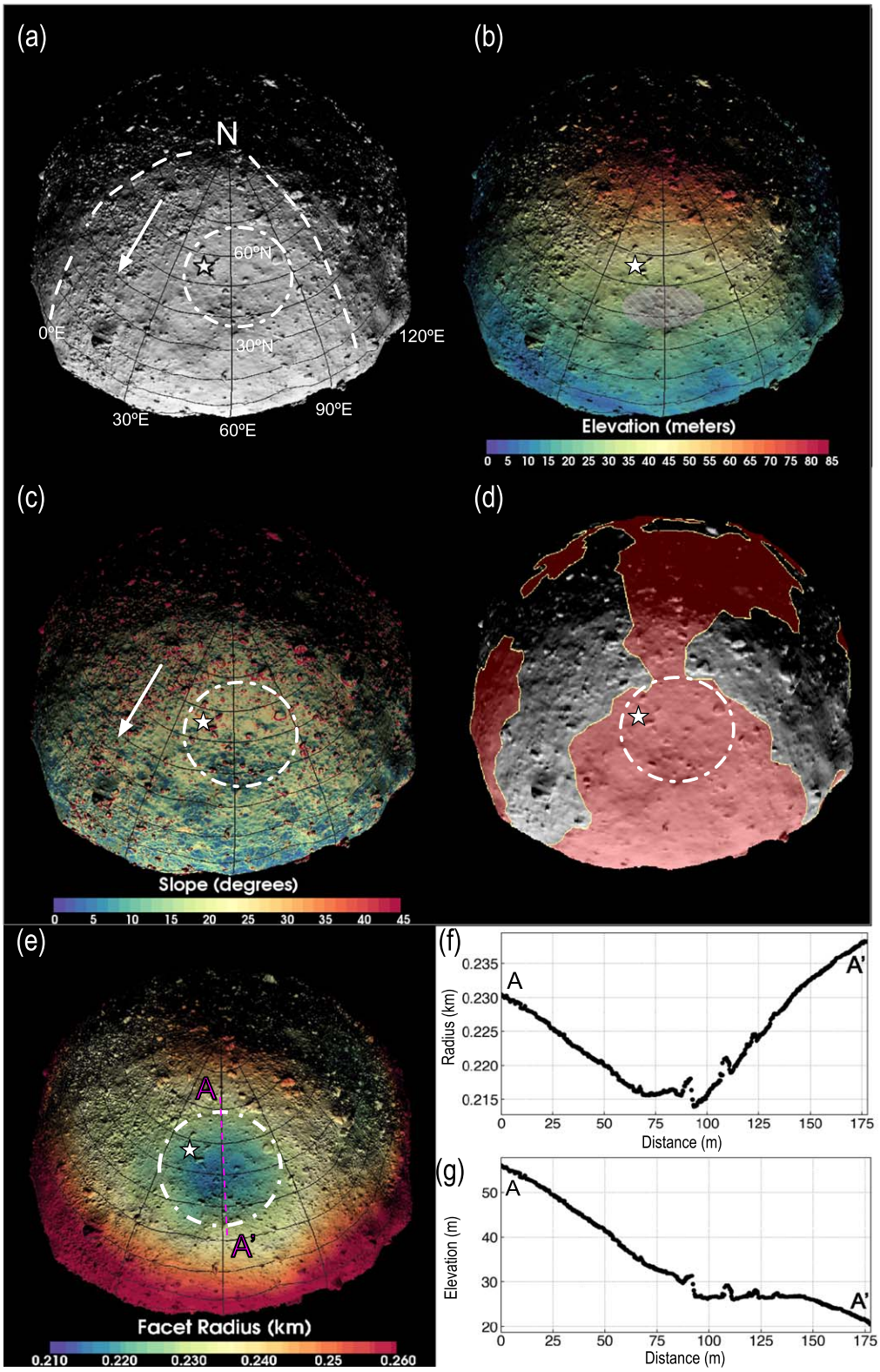

Figure 1. Northern view of the OLA GDTM (a) focusing on the Nightingale sample site and the Hokioi crater (star). The GDTM is overlaid with elevation relative to Bennu's (b) geoid, (c) slope, (d) geologic units (Smooth Unit in pink and Rugged Unit in gray; Jawin et al. 2022), and (e) radius (i.e., distance to the facet from the center of figure). Notable features providing global context for the Nightingale site include longitudinal ridges (dashed lines in panel (a)), morphological evidence of a rock fall (long arrow in panels (a) and (c)), an unnamed ∼120 m crater enclosing Hokioi and Nightingale (dotted–dashed circle in panels (a), (c), (d), and (e)), and an area of high boulder density (gray hash in panel (b)). The profile of the 120 m crater (dashed magenta line in panel (e)) is shown in radius from center (panel (f)) and elevation (panel (g)).

(blue and magenta in Figures 3(c) and (d)) using the LDTM. The blue profile (Figure 3(c)) shows the boulder topography along its longest axis, which measures ∼12 m, more than half the size of Hokioi crater. In the blue profile, we find two large cavities that measure approximately 1.5 and 4.8 m. We highlight the larger of these cavities with black dashed and

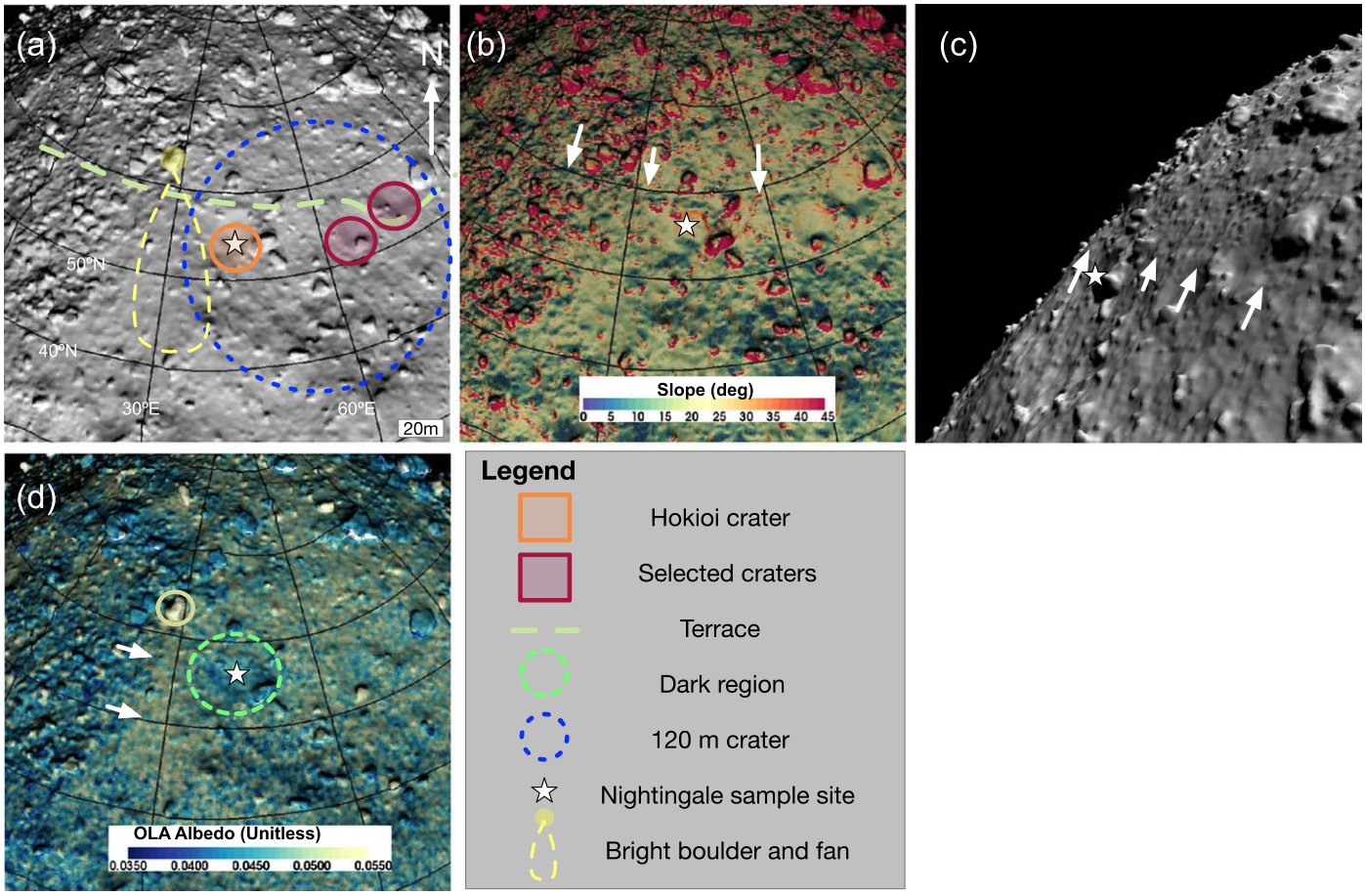

Figure 2. Regional area of Hokioi crater shown on the GTDM overlaid with (a) notation of features, (b) slope, and (d) OLA albedo measurements. The terrace, several craters of comparable size to Hokioi, a bright deposit apparently associated with a bright boulder, and a dark region surrounding the Hokioi crater are indicated. Arrows in panel (b) and the side view (panel (c)) show the slope break associated with the terrace mapped in panel (a). Arrows in panel (d) point to the bright deposit; the bright boulder is circled.

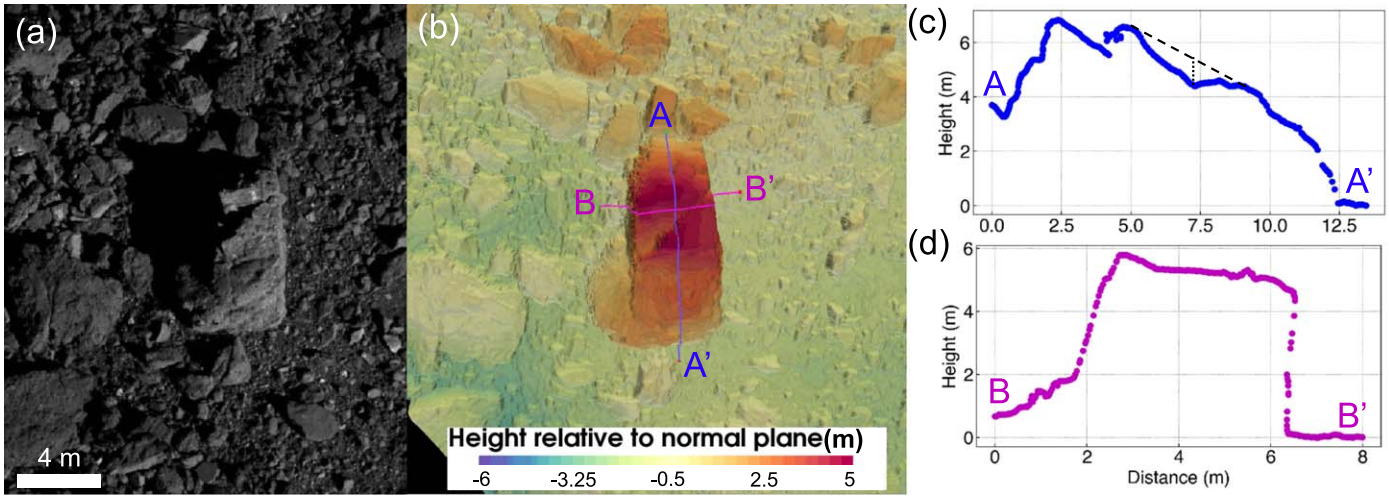

Figure 3. (a) Close-up PolyCam image (~5 cm pixel^{-1}) and (b) LDTM (0.05 m GSD) of the bright boulder. The blue and magenta profiles overlaid on the topographic data in panel (b) are shown in panels (c) and (d). The blue profile indicates a probable impact crater on the boulder (black dashed and dotted lines). The magenta profile shows the flat edges of the boulder, reminiscent of fracture planes.

dotted lines in Figure 3(c). This cavity is reminiscent of other craters on boulders on Bennu cataloged by Ballouz et al. (2020). The cavity has a depth-to-diameter (d/D) ratio of approximately 0.2, suggesting an impact origin (e.g., Marchi et al. 2015). Additional evidence comes from the boulder's topographic profile along its shortest axis (~4 m), shown by the magenta profile (Figure 3(d)). The steep sidewalls of the boulder probably represent smooth fracture planes, likely generated by the impact that created the crater shown in the blue profile. The diameter of the crater is sufficiently large that

the impact could have disrupted a boulder more than twice the size of the one we currently observe (Ballouz et al. 2020), leaving behind only this steep-sided remnant. The production of debris from a comparatively bright boulder on Bennu is also supported by the findings of Cambioni et al. (2021), who showed that Bennu's lower-porosity boulders—which are also its higher-reflectance boulders (DellaGiustina et al. 2020; Rozitis et al. 2020)—are the dominant source of in situ regolith generation. We therefore conclude that an impact catastrophically disrupted a larger bright boulder in place, leaving behind the observed 12 m remnant and generating smaller fragments that would have been swept downslope by creep processes, creating the observed bright deposit.

The terrace and bright deposit further provide evidence that the surface of Bennu is likely unstable in this steep region near 55° N latitude (Section 3). Material probably migrates continuously through the Nightingale site from the north toward the equator. Given that the terrace spans both rugged and smooth terrains, this migration may be very recent. The bright deposit seems to show no increase in accumulation at the terrace slope break; it may have formed before the terrace existed and has continued to grow thereafter.

Although we have presented several lines of evidence for downslope migration of surface material in the region of the Nightingale sample site, this does not put into question the older surface age of the Smooth Unit in which it resides (Jawin et al. 2022), relative to the Rugged Unit, because that age assessment is based primarily on the relative concentrations of craters with diameters <20 m. The surface motion that we infer in this area is apparently insufficient to erase craters of 20 m in diameter (as evinced by the presence of Hokioi and other similarly sized craters) or alter the overall appearance of the Smooth Unit, and therefore it is likely limited to the top meter of the surface.

Hokioi crater appears to be the youngest of the three ∼20 m diameter craters located in the region (Figure 2(a)). In terms of OLA albedo, Hokioi sits in a relatively bright region, but the crater itself and its immediate surroundings are darker, which could mean that they are rougher based on the information captured by this data type (Section 2.2). However, by using the global image mosaic (Bennett et al. 2021) and a local DTM, we determined that the low observed OLA albedo values (Figure 2(c)) are in fact due to the darkness of the terrain, not a consequence of the texture of surface, which is fine-grained (particles <0.05 m diameter).

The distribution of the dark fine material (Figure 4), in both the crater and its immediate surroundings, is reminiscent of ejecta deposits seen in other planetary environments, which tend to be finer than the surrounding material (e.g., Schultz & Mendell 1978). This material superposes the bright deposit (Figure 2(d)). We therefore infer that the area of low OLA albedo around Hokioi consists of impact ejecta. Ejecta have also been observed elsewhere on Bennu, at Bralgah crater (Perry et al. 2022), and ejecta excavation and deposition were observed on Ryugu during an impact experiment by the Hayabusa2 mission (Arakawa et al. 2020). The presence of dark patches in the OLA albedo data may indicate that Hokioi crater is inverting the stratigraphy, exposing a finer, darker, and fresher subsurface located at depth. The two similarly sized craters (Figure 2(a)) to the east are also somewhat darker than the surrounding bright terrain, but not as dark as the material inside and around Hokioi crater. These two craters do not have dark deposits around them (Figure 2(c)), indicating that any ejecta deposits have been degraded and have a more subdued shape. Based on these observations, we infer that these two craters are older than Hokioi.

These interpretations of the OLA albedo data are supported by previous analyses of data collected by OCAMS and OVIRS, which showed Hokioi crater to be the reddest crater and among the darkest areas relative to average Bennu (DellaGiustina et al. 2020; Deshapriya et al. 2021; Rizos et al. 2021). DellaGiustina et al. (2020) argued that the reddest craters are likely the freshest and could have formed within the past ∼100,000 yr. Therefore, Hokioi crater is probably one of the freshest craters on Bennu.

5. Local Context of the Nightingale Site

Viewing Hokioi crater in a 0.05 m GSD OLA LDTM in perspective (Figure 5(a)) shows that the OSIRIS-REx Touch-And-Go (TAG) sampling mechanism (Bierhaus et al. 2018) collected material from a broad topographic feature located on the crater floor consistent with a slump or mass flow deposit. The slump's surface shows evidence for several distinct flows that are superposed on one another, indicating discrete slope failures (Figure 6(d)). These features start primarily from the northeastern quadrant of the crater rim and wall and flow across the crater toward the south−southwest. The slopes of the crater wall range from ∼30° in the west to ∼40° in the north −northwest to northeast. Prior to the slump, these slopes were likely steeper, especially in the north−northeastern portions, and probably collapsed either immediately after crater formation or during increases in regional slope due to YORP-driven spin-up. Both processes could explain the multiple apparent lobes on the crater floor. PolyCam images of the crater interior also show evidence of possibly ongoing small-scale creep where the crater wall is now the steepest (Figures 6(a) and (b)), near the current maximum slope of $40° \pm 10°$. In contrast to our observations of Bennu, wall slumping on Ryugu has been observed only in its largest crater, Urashima (Sugita et al. 2019; Cho et al. 2021).

The even more detailed SPO LDTM (Figure 7), which resolves surface heights at a GSD of 0.01 m, shows that, though smoother than many other areas of Bennu, the OSIRIS-REx contact point is not perfectly so and includes rocks up to 0.05 m in height relative to the surrounding terrain. The SPO LDTM also indicates that the local slope at the contact point is 8°–10° shallower than the steepest portions of the crater wall, at ∼29°. The observed variations in surface height (Figures 7(b)–(c)) come from the mix of rocks and fines sourced from the Hokioi crater wall and beyond. Some of these granular flows likely include late-stage Hokioi ejecta.

OCAMS images (e.g., Figure 6) indicate that much of the slump in the central portion of the crater interior is dark, redder than average (DellaGiustina et al. 2020; Rizos et al. 2021), and fine-grained (⩽0.05 m; Burke et al. 2021). OLA albedo confirms the darkness of the slump (Figure 5(b)). Much of the fine-grained material in the central slump deposit can be visually classified as angular to subangular (Figure 8). OCAMS images also show a few isolated larger rock fragments that vary in reflectance (Burke et al. 2021). OLA albedo confirms this OCAMS finding and indicates that brighter material is especially present to the north and west of the Nightingale sample site, on the walls and floor of Hokioi crater (Figure 5(b)). The OLA and OCAMS data sets both indicate

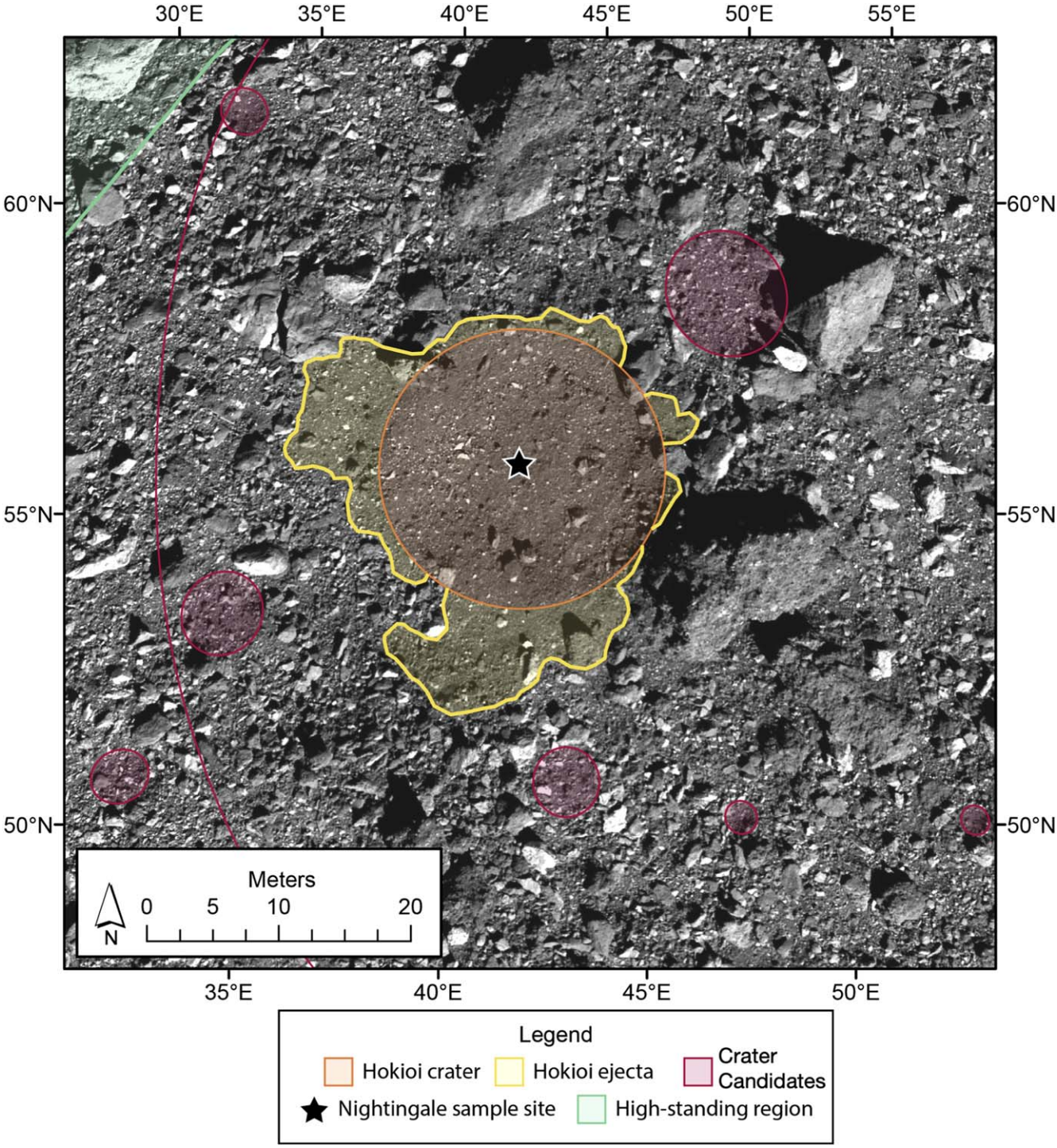

Figure 4. Sketch map of the Nightingale region, including Hokioi crater (orange outline), small candidate craters (red outlines with shading), the 120 m crater in which Hokioi is located (long red outline on the western side of Hokioi), and the edge of an adjacent high-standing region (green outline). Fine-grained deposits surrounding the crater (yellow) are interpreted to be crater ejecta. The basemap over which these features are annotated is from the global image mosaic (Bennett et al. 2021), in sinusoidal projection.

that surface creep observed in the crater (Figure 6(b)) is bringing surrounding bright material from the north and north −northeastern flanks of the Hokioi crater wall and floor, and that some of this bright material was probably present at the contact point. The slow modification and accompanied brightening by surface creep that this evidence implies probably contribute to the higher OLA albedo of the two other nearby ∼20 m diameter craters. Longer exposures to space weathering relative to Hokioi crater are another contributing factor (DellaGiustina et al. 2020; Rizos et al. 2021).

6. Discussion

We infer that the Nightingale sample site experienced several periods of geologic activity before it was sampled by the OSIRIS-REx spacecraft. This activity has bearing on the origin

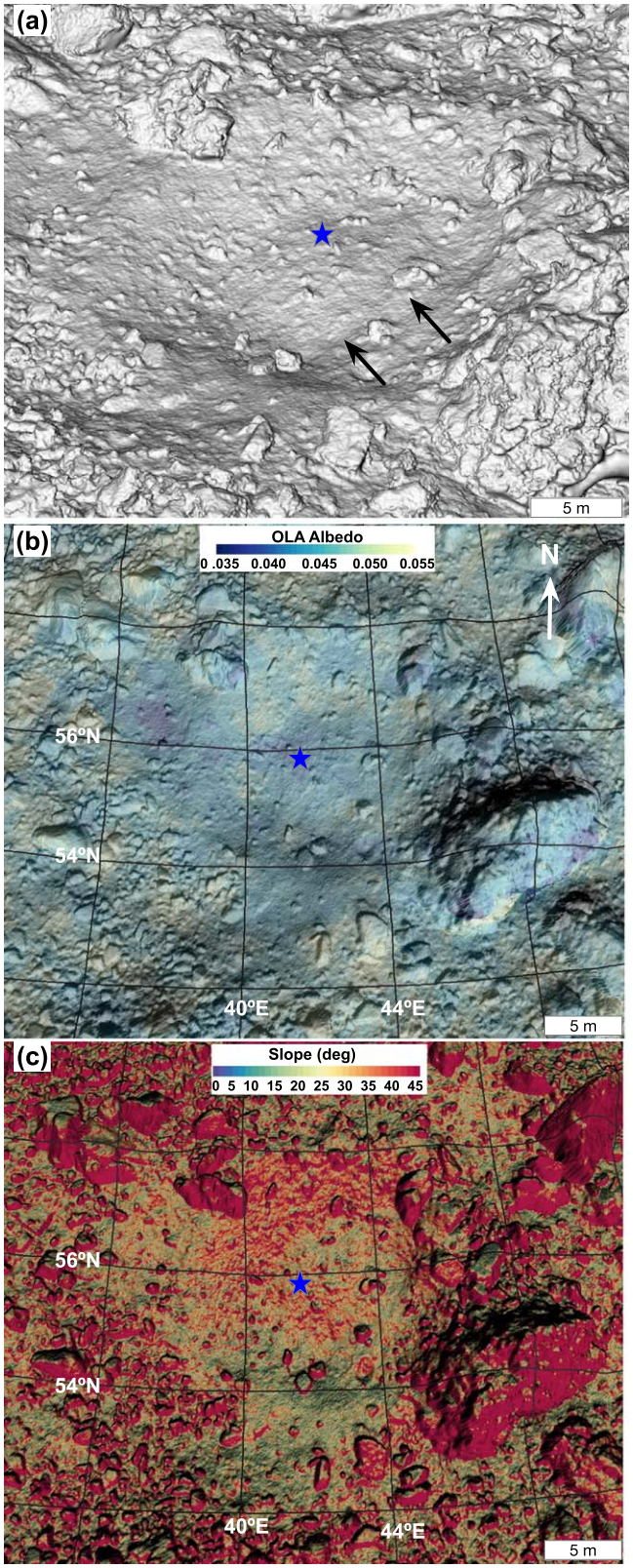

Figure 5. A 0.05 m GSD OLA LDTM illustrating the detailed morphology of the Nightingale site within Hokioi crater, including (a) an interior slump (black arrows), (b) OLA albedo, and (c) slopes. Panel (a) views the LDTM obliquely; panels (b) and (c) view it from above. The point on the surface where the OSIRIS-REx sampling mechanism made contact is indicated with a star.

and contents of the sample that OSIRIS-REX will return to Earth in 2023. The geologic history (Figure 9) of the Nightingale site begins with the formation of the longitudinal ridges. These ridges limit the extent to which material in this area can migrate across the asteroid from east and west. After the ridges formed, possibly from an earlier spin-up event in which Bennu was nearly disrupted (Daly et al. 2020a), or interior aggregates readjusted (Zhang et al. 2022), an impact created a ∼120 m crater that excavated and exposed Bennu's subsurface. Although not apparent, it is highly likely that ejecta was deposited beyond the rim of the 120 m crater, given the observations of ejecta at Hokioi (Figure 3) and Bralgah (Perry et al. 2022) craters. This ejecta has since become indistinguishable from the surrounding terrain owing to the cumulative effect of processes such as impact gardening, surface creep, and space weathering, which for carbonaceous chondrites leads to surface brightening (e.g., DellaGiustina et al. 2020; Deshapriya et al. 2021; Rizos et al. 2021). Some of this ejecta accumulated in the 120 m crater as it slowly became a regional sedimentary basin.

The 120 m crater probably formed before the elongate accumulation of boulders to the west, given that this accumulation seems to be shaped in part by the crater rim. The elongate accumulation of boulders is likely a product of the increases in Bennu's spin rate leading to steepened slopes and surface instabilities, which in part contributed to the creation of the Rugged Unit. Bennu's spin rate has continued to increase since the time those units formed, resulting in regional and localized surface failures expressed as the fan-like deposit of bright rock fragments and the creep-induced terrace just north of the sample site. During this period, impacts formed smaller (∼20 m) craters within the 120 m crater, which exposed darker, finer, and less space-weathered underlying material and probably generated ejecta. Since their formation, these craters have brightened over time owing to a combination of space weathering and migration of bright material into their interiors, and evidence of ejecta has been lost for all but Hokioi, which is the youngest.

The sample, therefore, should be primarily composed of two main components. Most of the sample is likely the darker and finer material that dominates the inside of Hokioi crater. Based on Hokioi's diameter, this dark material is plausibly excavated from the top meter and a half of the surface of Bennu, as expected for a simple bowl-shaped crater (e.g., Gault et al. 1968; Stoeffler et al. 1975). This dark, relatively fresh material should be accompanied, but in lesser volume, by material from the surrounding brighter and older terrain, that is, the Smooth Unit. This second component will possess individual grains that are more angular than the finer dark constituent and, therefore, likely to be stronger. Their increased strength follows the results obtained from thermal inertia (Rozitis et al. 2020), which finds that these angular grains possess less microporosity (Rozitis et al. 2020). These grains might also contain some of the carbonates identified in Hokioi crater and its surroundings (Kaplan et al. 2020). Alternatively or in addition, it might include some fragments of the rare, very bright exogenic basalts identified globally across Bennu that are proposed to have originated from Vesta or the vestoids (DellaGiustina et al. 2021). A substantial portion of the sample may be material that was originally excavated within the top ∼10 m of Bennu's surface by formation of the unnamed 120 m crater in which Hokioi crater is located, again as expected for ejecta excavated from a simple crater (e.g., Gault et al. 1968; Stoeffler et al. 1975).

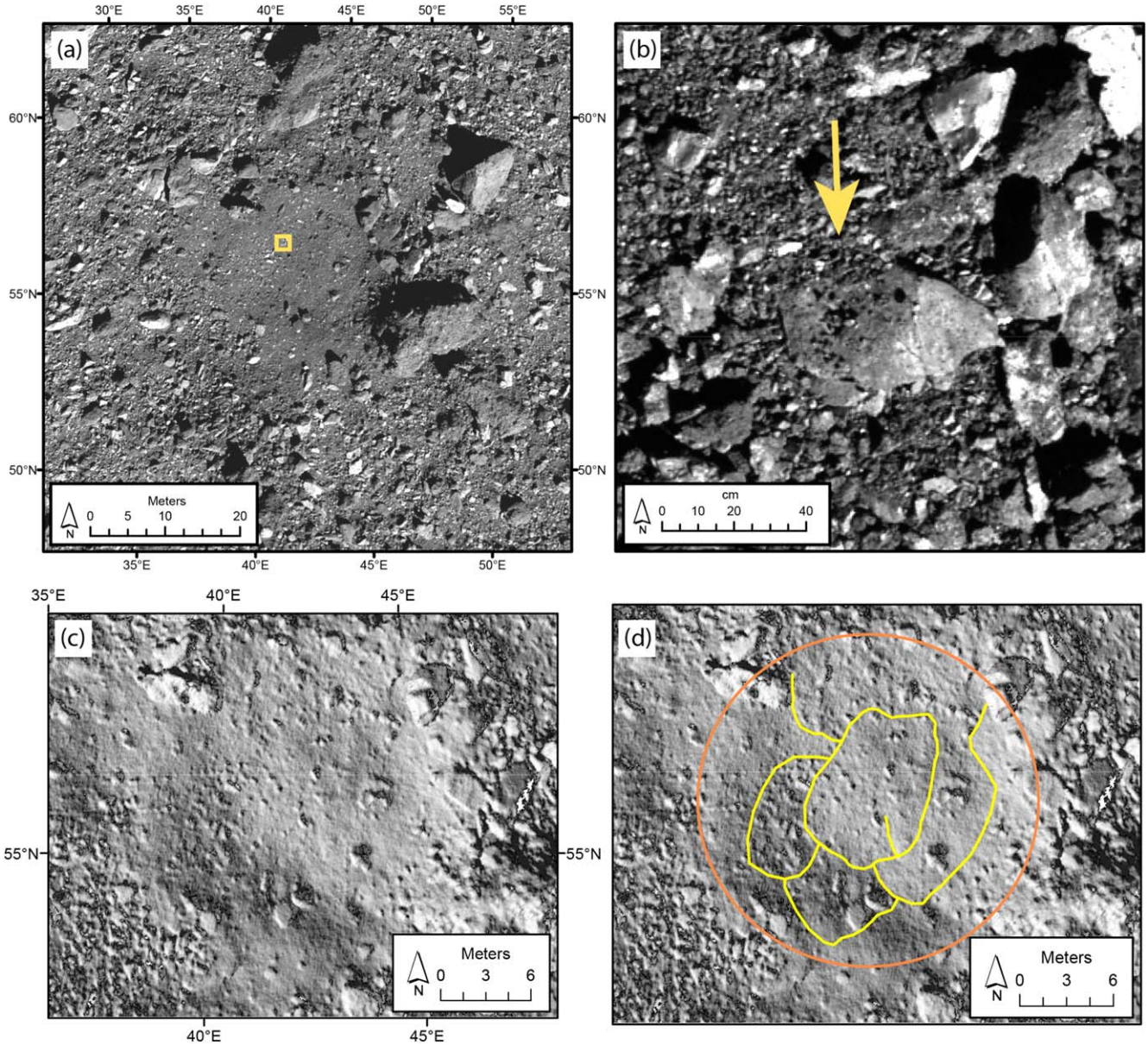

Figure 6. Example of creep inside Hokioi crater, consistent with mass movement downslope toward the south. (a) Context image of Hokioi crater from the global image mosaic (Bennett et al. 2021), in sinusoidal projection. The yellow box shows the extent of panel (b). (b) The yellow arrow indicates particles that have mantled a larger boulder owing to creep toward the south (from PolyCam image ocams20200303t211013s895; pixel scale, 0.0036 m; phase angle, 56°). The crater wall slope in this area is 40° based on the OLA DTM shown in Figure 5. (c) 0.5 m GSD LDTM of Hokioi crater. (d) Yellow outlines indicate subtle lobate features (see also the oblique perspective in Figure 5(a)) indicating surface slumps and material migration toward the south. Several events may have occurred, leading to the multiple lobate features. The orange circle approximately indicates the crater rim.

The slump within Hokioi crater likely resulted from collapse of the northeastern rim of the crater during or after Hokioi's formation, because of the low cohesive nature of the regolith. Such collapse would have included the late-stage crater ejecta apparent around the crater in OCAMS and OLA data. Assuming a typical impact velocity of 5 km s^{-1} for near-Earth asteroids such as Bennu (Bottke et al. 1994), this ejecta would be expected to include small but detectable (at the few percent level) amounts of projectile material (e.g., Daly & Schultz 2018). The sample returned by OSIRIS-REx could therefore include material from the projectile that generated Hokioi crater specifically, in addition to the vestoid exogenic material more generally strewn across Bennu's surface. The projectile that formed Hokioi is unlikely to be an exogenic basalt given the inferred very young age of this crater, which implies that it was produced when Bennu was already in the near-Earth space. It is more likely that a more common type of asteroidal material in the near-Earth asteroid population, maybe S-type or C-type, created this crater within the past ~100,000 yr (DellaGiustina et al. 2020; Jawin et al. 2022). Recent analyses of anhydrous, exogenous boulders on Bennu show that most appear to be V types (Le Corre et al. 2021; Tatsumi et al. 2021), but dynamical analyses indicate that these were likely inherited from impacts to Bennu's parent body, rather than impacts directly to Bennu itself (DellaGiustina et al. 2021).

Nightingale has some similarities with the sites on Ryugu that were sampled by the Hayabusa2 mission (Arakawa et al. 2020; Morota et al. 2020). Specifically, both missions sampled regions of their respective asteroids that have been recently

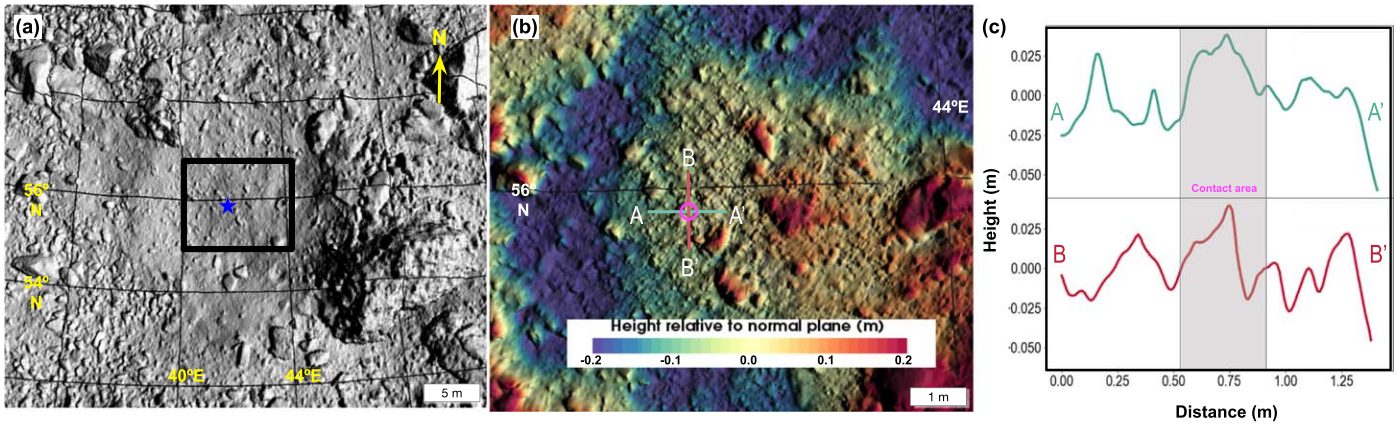

Figure 7. (a) Location (black box) in the 0.05 m OLA LDTM (Figure 5) of (b) the 0.01 m GSD SPO LDTM of the Nightingale site. (c) Surface height profiles at the OSIRIS-REx contact area (magenta circle).

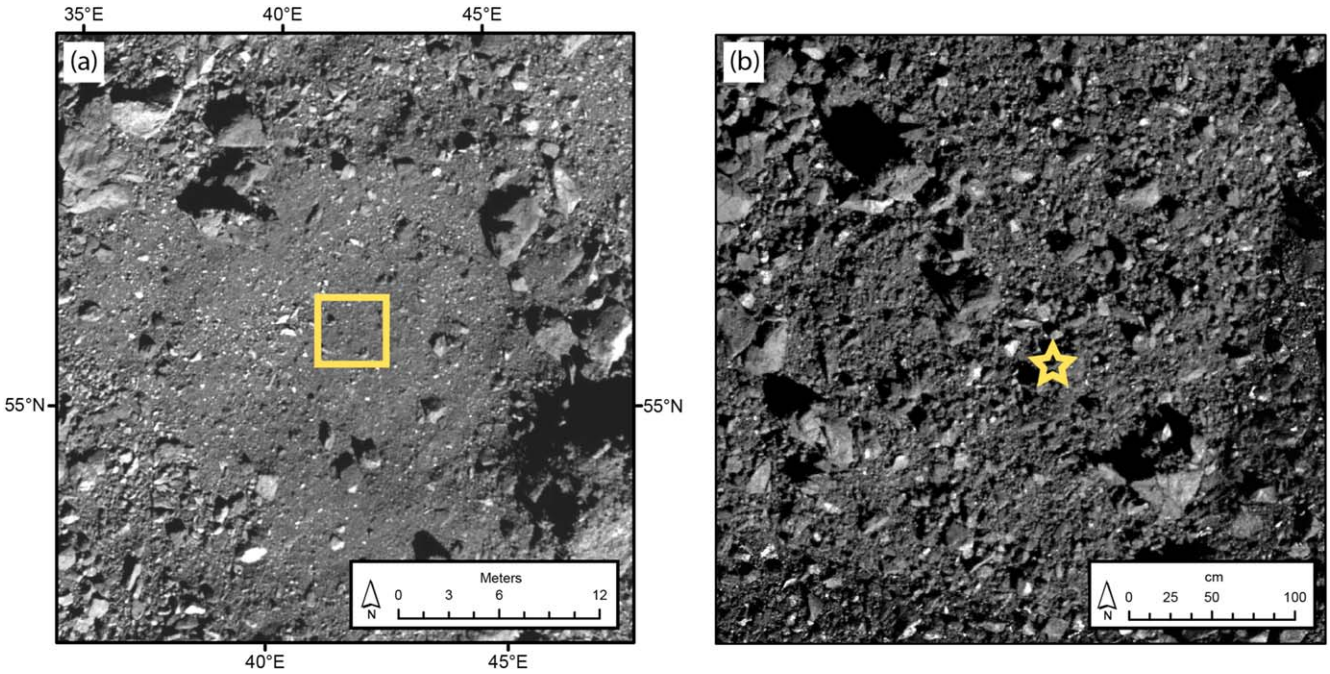

Figure 8. Textures near the Nightingale sample site. (a) Context image of Hokioi crater from the global image mosaic (Bennett et al. 2021), in sinusoidal projection. The yellow box shows the extent of panel (b). (b) The region surrounding Nightingale contains a mixture of angular to subangular rock fragments and fine-grained material. Albedo variations are also apparent. The yellow star indicates the OSIRIS-REx contact point. From PolyCam image ocams20200303t210644s436 (pixel scale, 0.003 7 m; phase angle, 56°).

exposed by geophysical processes. Based on color units on Ryugu, the equatorial region—where the sample sites are located—has recently experienced mass wasting toward the midlatitudes, which is the geopotential low on Ryugu (Sugita et al. 2019). However, the different latitudes of the sample sites on Bennu and Ryugu (high-latitude versus equatorial) may mean that the samples will have experienced different degrees of space weathering.

The fact that flows (Figure 6(d)) on the central slump of Hokioi crater (Figure 5(a)) come to a stop on an ∼29° slope where OSIRIS-REx contacted the surface provides constraints on the static friction angle of the surface material collected. Many investigations show that for granular materials (e.g., Hunger & Morgenstern 1984; Cheng & Zhao 2017; Al-Hashemi & Al-Amoudi 2018, and references therein) the angle at which a flow comes to a stop is usually about 3°–10° smaller than the static friction angle of the material. In such moving flows of a mass column, cohesion forces are not expected to be important, as the weight of individual particles in the granular system likely exceeds the cohesive forces present (Castellanos 2005); otherwise, motion could not have been initiated. Per Coulomb's friction model (e.g., Iverson & Reid 1997), when friction alone leads to flow stoppage, gravity differences between the Earth and Bennu are not expected to be important. The sample collected, therefore, should have a friction angle between 32° and 39°. This range of angles is consistent with inferences one would make based on the observed subangular to angular morphology of individual rocks present in Hokioi crater. The shapes of these rocks compare well to those of gravel or rough sand particles, which have angles of friction $\geqslant 35°$. In comparison, more rounded particles like glass beads or smooth sand particles have friction angles $\leqslant 22°$ (Ballouz et al. 2021, and references therein).

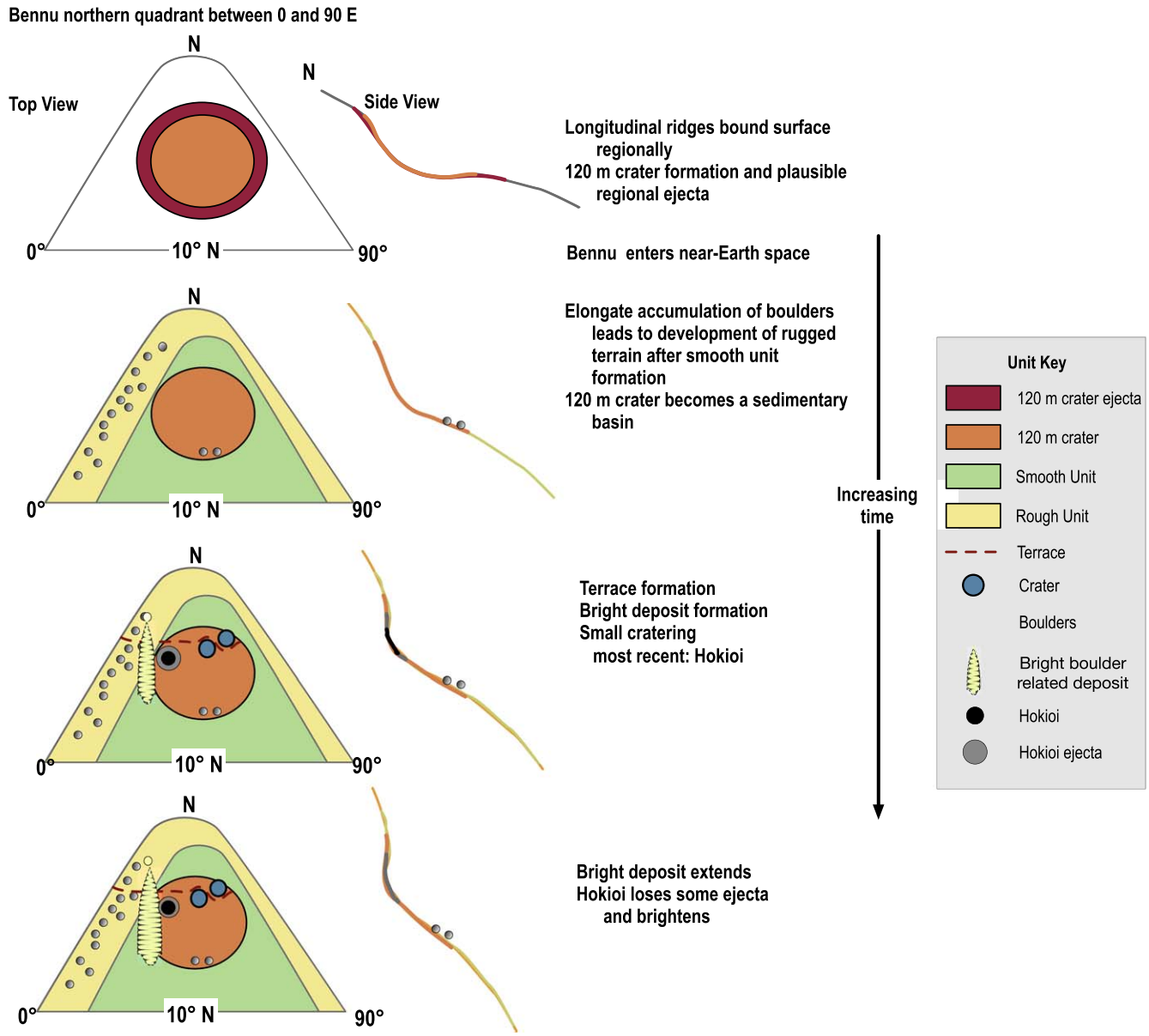

Figure 9. Schematic of the geological history of the Nightingale sample site. The schematic approximates the region of Bennu shown in Figure 2.

Given this estimated friction angle, the surface strength and cohesion of the samples are likely small. Based on evidence from the larger Bralgah crater, near 45° S, 325° E, which is surrounded by an expansive ejecta blanket (Perry et al. 2022), the surface yield strength at Hokioi crater is <100 Pa. An investigation of the origins of terraces on Bennu (Barnouin et al. 2022) indicated that the cohesion could be as small as 0.2 (0.6) Pa for surface regolith thicknesses of 3 (10) m. Here, we apply the same slope stability analyses as used in Barnouin et al. (2022), where the resisting frictional and cohesive stresses to gravity are given by

$$\mathrm{FS} = \frac{\tan\phi}{\tan\theta} + \frac{c}{\gamma_t T \sin\phi}, \tag{1}$$

where θ is the slope angle, ϕ is the frictional angle of the surface material, c is the cohesion, γ_t is the depth-averaged total unit weight (layer bulk density times the local acceleration due to gravity), and T is the thickness of the unconsolidated surface layer (mixture of boulders and regolith) that could fail. Equation (1) applies to thin flows. Values <1 of this factor of safety, FS, imply that the slope is prone to failure. To estimate the cohesion of the surface material in Hokioi crater, we use the range of static friction angles estimated here and the global bulk density of Bennu (1194 ± 3 kg m^{-3}; Daly et al. 2020a). We assume a 0.05 m thickness for the particles mantling the boulder in Figure 6(b), which is thin relative to the meters-long crater wall and provides evidence for surface failure (i.e., for FS $\leqslant 1$). With the measured 40° wall slope of Hokioi crater, we find that the cohesion of the surface material could be as small as 0.0001–0.007 Pa.

7. Conclusion

We present a geological and geotechnical assessment of the Nightingale sample site on Bennu prior to its disturbance by the

OSIRIS-REx sampling event. This analysis constrains the expected sources and properties of the sample to be returned:

1. The sample is primarily derived from material caught between two longitudinal ridges located near 0° and 90°, from a smooth geologic unit that predates when Bennu became a near-Earth asteroid and is more stable than nearby rugged surface units. Some material may have been excavated from as deep as 10 m within Bennu when the regional 120 m crater formed.
2. The bulk of the sample will be fresh, spectrally redder than average Bennu, dark (DellaGiustina et al. 2020; Deshapriya et al. 2021; Rizos et al. 2021), fine-grained (<0.05 m), excavated from <1.5 m depth, and exposed recently (maybe within the past 100,000 yr) during the formation of Hokioi crater.
3. The second most dominant material within the sample will be derived from the brighter regolith surrounding Hokioi crater and may include carbonates (Kaplan et al. 2020) and/or exogenic basalts of possible vestoid origin (Kaplan et al. 2020; DellaGiustina et al. 2021). These brighter materials became trapped within the Nightingale site as a result of surface processes that drive regolith slowly from the north pole toward the equator of Bennu. Individual grains of this material are likely stronger and less porous than their darker counterparts.
4. A small fraction of the sample will consist of exogenic material from the projectile that formed Hokioi crater. This material likely differs from the bright exogenic basalts observed globally (DellaGiustina et al. 2021; Le Corre et al. 2021; Tatsumi et al. 2021) on Bennu.
5. The static friction angle of the bulk sample will likely be between 32° and 39°. Any sample shaking during reentry may reduce this angle.
6. The cohesion of the bulk sample will be small, well below 100 Pa and somewhere between 0.6 and 0.0001 Pa. This very low cohesion may be difficult to measure in 1 g on Earth.

This effort was supported by NASA under contract NNM10AA11C issued through the New Frontiers Program and by the Canadian Space Agency. All data from the OSIRIS-REx mission are available via the Planetary Data System at https://sbn.psi.edu/pds/resource/orex/. Global DTMs of Bennu produced from radar and flight data are available via the Small Body Mapping Tool at http://sbmt.jhuapl.edu/. P.M. and Y.Z. acknowledge funding support from the French space agency CNES and from Academies of Excellence: Complex Systems and Space, Environment, Risk, and Resilience, part of the IDEX JEDI of the Université Côte d'Azur.

ORCID iDs

O. S. Barnouin https://orcid.org/0000-0002-3578-7750
E. R. Jawin https://orcid.org/0000-0002-2341-8819
R. T. Daly https://orcid.org/0000-0002-1320-2985
R.-L. Ballouz https://orcid.org/0000-0002-1772-1934
M. G. Daly https://orcid.org/0000-0002-3733-2530
P. Michel https://orcid.org/0000-0002-0884-1993
Y. Zhang https://orcid.org/0000-0003-4045-9046
C. L. Johnson https://orcid.org/0000-0001-6084-0149
K. J. Walsh https://orcid.org/0000-0002-0906-1761
M. M. Al Asad https://orcid.org/0000-0001-8209-858X
R. Gaskell https://orcid.org/0000-0002-2293-7879
J. Weirich https://orcid.org/0000-0002-2830-1708
E. Palmer https://orcid.org/0000-0001-6755-8736
E. B. Bierhaus https://orcid.org/0000-0001-5890-9821
M. C. Nolan https://orcid.org/0000-0001-8316-0680
D. S. Lauretta https://orcid.org/0000-0002-2597-5950

References

Al-Hashemi, H. M. B., & Al-Amoudi, O. S. B. 2018, Powder Technology, 330, 397
Arakawa, M., Saiki, T., Wada, K., et al. 2020, Sci, 368, 67
Ballouz, R. L., Walsh, K. J., Barnouin, O. S., et al. 2020, Natur, 587, 205
Ballouz, R. L., Walsh, K. J., Sánchez, P., et al. 2021, MNRAS, 507, 5087
Barnouin, O. S., Daly, M. G., Palmer, E. E., et al. 2019, NatGe, 12, 247
Barnouin, O. S., Daly, M. G., Palmer, E. E., et al. 2020, P&SS, 180, 104764
Barnouin, O. S., Daly, M. G., & Seabrook, J. A. 2022, JGRE, in press
Barnouin-Jha, O. S., Cheng, A. F., Mukai, T., et al. 2008, Icar, 198, 108
Bennett, C. A., DellaGiustina, D. N., Becker, K. J., et al. 2021, Icar, 357, 113690
Bierhaus, E. B., Clark, B. C., Harris, J. W., et al. 2018, SSRv, 214, 107
Bierhaus, E. B., Trang, D., Daly, R. T., et al. 2022, NatGe, in press
Bos, B. J., Nelson, D. S., Pelgrift, J. Y., et al. 2020, SSRv, 216, 71
Bos, B. J., Ravine, M. A., Caplinger, M., et al. 2018, SSRv, 214, 37
Bottke, W. F., Nolan, M. C., Greenberg, R., & Kolvoord, R. A. 1994, Icar, 107, 255
Burke, K. N., DellaGiustina, D. N., Bennett, C. A., et al. 2021, RemS, 13, 1315
Cambioni, S., Delbo, M., Poggiali, G., et al. 2021, Natur, 598, 49
Castellanos, A. 2005, AdPhy, 54, 263
Cheng, A. F., Barnouin, O. S., Prockter, L., et al. 2002, Icar, 155, 51
Cheng, N.-S., & Zhao, K. 2017, International Journal of Sediment Research, 32, 149
Cho, Y., Morota, T., Kanamaru, M., et al. 2021, JGRE, 126, e06572
Christensen, P. R., Hamilton, V. E., Mehall, G. L., et al. 2018, SSRv, 214, 87
Daly, M. G., Barnouin, O. S., Dickinson, C., et al. 2017, SSRv, 212, 899
Daly, M. G., Barnouin, O. S., Seabrook, J. A., et al. 2020a, SciA, 6, 41
Daly, R. T., Bierhaus, E. B., Barnouin, O. S., et al. 2020b, GeoRL, 47, e89672
Daly, R. T., & Schultz, P. H. 2018, SciA, 4, eaar2632
DellaGiustina, D. N., Burke, K. N., Walsh, K. J., et al. 2020, Sci, 370, eabc3660
DellaGiustina, D. N., Emery, J. P., Golish, D. R., et al. 2019, NatAs, 3, 341
DellaGiustina, D. N., Kaplan, H. H., Simon, A. A., et al. 2021, NatAs, 5, 31
Deshapriya, J. D. P., Barucci, M. A., Bierhaus, E. B., et al. 2021, Icar, 357, 114252
Gaskell, R. W., Barnouin-Jha, O. S., Scheeres, D. J., et al. 2008, M&PS, 43, 1049
Gault, D. E., Quaide, W. L., & Oberbeck, V. R. 1968, in in Shock Metamorphism of Natural Materials, ed. B. M. French & N. M. Short (Baltimore: Mono Book Corp), 87
Golish, D. R., Drouet d'Aubigny, C., Rizk, B., et al. 2020, SSRv, 216, 12
Hamilton, V. E., Christensen, P. R., Kaplan, H. H., et al. 2021, A&A, 650, A120
Hamilton, V. E., Simon, A. A., Christensen, P. R., et al. 2019, NatAs, 3, 332
Hergenrother, C. W., Maleszewski, C. K., Nolan, M. C., et al. 2019, NatCo, 10, 1291
Hunger, O., & Morgenstern, N. R. 1984, Géotechnique, 34, 405
Iverson, R. M., & Reid, M. E. 1997, AREPS, 25, 85
Jawin, E. R., McCoy, T. J., Walsh, K. J., et al. 2022, Icar, in press
Jawin, E. R., Walsh, K. J., Barnouin, O. S., et al. 2020, JGRE, 125, e06475
Kaplan, H. H., Lauretta, D. S., Simon, A. A., et al. 2020, Sci, 370, eabc3557
Lauretta, D. S., DellaGiustina, D. N., Bennett, C. A., et al. 2019, Natur, 568, 55
Lauretta, D. S., Enos, H. L., Polit, A. T., Roper, H. L., & Wolner, C. W. V. 2021, in in Sample Return Missions, ed. A. Longobardo (Amsterdam: Elsevier), 163
Le Corre, L., Reddy, V., Bottke, W. F., et al. 2021, PSJ, 2, 114
Marchi, S., Chapman, C. R., Barnouin, O. S., Richardson, J. E., & Vincent, J. B. 2015, in Asteroids IV, ed. P. Michel, F. E. Demeo, & W. F. Bottke (Tucson, AZ: Univ. Arizona Press), 725
Masterson, R. A., Chodas, M., Bayley, L., et al. 2018, SSRv, 214, 48
Michel, P., Ballouz, R. L., Barnouin, O. S., et al. 2020, NatCo, 11, 2655
Morota, T., Sugita, S., Cho, Y., et al. 2020, Sci, 368, 654
Neumann, G., Barker, M., Mazarico, E., et al. 2020, LPSC, 51, 2032
Nolan, M. C., Howell, E. S., Scheeres, D. J., et al. 2019, GeoRL, 46, 1956

Perry, M. E., Barnouin, O. S., Daly, R.T., et al. 2022, NatGe, in press
Reuter, D. C., Simon, A. A., Hair, J., et al. 2018, SSRv, 214, 54
Rizk, B., Drouet DAubigny, C., Golish, D., et al. 2018, SSRv, 214, 26
Rizos, J., de León, J., Licandro, J., et al. 2021, Icar, 364, 114467
Roberts, J. H., Barnouin, O. S., Daly, M. G., et al. 2021, P&SS, 204, 105268
Rozitis, B., Ryan, A. J., Emery, J. P., et al. 2020, SciA, 6, eabc3699
Rubincam, D. P. 2000, Icar, 148, 2
Scheeres, D. J., French, A. S., Tricarico, P., et al. 2020, SciA, 6, eabc3350
Scheeres, D. J., Hesar, S. G., Tardivel, S., et al. 2016, Icar, 276, 116
Scheeres, D. J., McMahon, J. W., French, A. S., et al. 2019, NatAs, 3, 352
Schultz, P. H., & Mendell, W. 1978, LPSC, 3, 2857
Simon, A. A., Kaplan, H. H., Hamilton, V., et al. 2020, Sci, 370, eabc3522
Stoeffler, D., Gault, D. E., Wedekind, J., & Polkowski, G. 1975, JGR, 80, 4062
Sugita, S., Honda, R., Morota, T., et al. 2019, Sci, 364, eaaw0422
Tatsumi, E., Popescu, M., Campins, H., et al. 2021, MNRAS, 508, 2053
Zhang, Y., Michel, P., Barnouin, O. S., et al. 2022, NatCo, submitted